UNIVERSITAT DE BARCELONA

# Spin crossover supramolecular coordination compounds: design, synthesis and properties

Mohanad D .Darawsheh

# Contents

# CHAPTER 5: Spin Crossover and Single Ion Magnet Behavior in Host-Guest Fe(II) Helicates

## 5.1 Introduction

A very interesting subarea in host-guest chemistry is the encapsulation of metal complexes inside the cavity of a metallosupramolecular cage. Fujita's research group has published several examples of such encapsulation. They have, for examples encapsulated classical metal complexes, *i.e.* $M^{II}(acac)_2$ (M = Pt, Pd or Cu; acac = acetylacetonato), inside a coordination cage. The Pd coordination cage has an organic-pillared framework with a large box-shaped hydrophobic cavity, which is ideal to bind two planar molecules.[1] The same group was able to encapsulate three planar metal porphirine or azaporphirine complexes inside another Pd coordination cage with a bigger cavity.[2] Also, the spin state of Ni(II)(acen) (acen = N,N`-ethylenebis(acetylacetoneiminato) and Co(II)(tap) (tap = tetraazaporphirinato) could be changed by encapsulation inside a coordination cage.[3] Another example of such metal complex encapsulation is the self-assembly of a $Cu_3$ trigonal-prismatic metallocage that encapsulates inside its cavity a $CuI_3^{2-}$ metal complex.[4] One of the possible applications of metal complex encapsulation is the targeted drug delivery. Cisplatine-like drugs and other biological relevant guests were encapsulated inside several metallosupramolecular cages where the metal of the cages are normally Pd(II) or Ru(II) ions.[5–9]

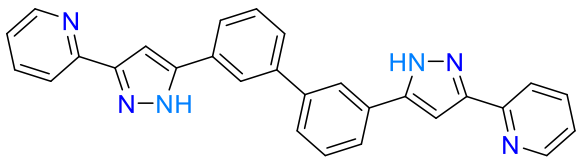


**Figure 5.1**: 3,3'-bis(3-(pyridin-2-yl)-1H-pyrazol-5-yl)-1,1'-biphenyl (H2L6).

In chapter 2, the encapsulation of $ClO_4^-$ inside the helical cavity of $[Fe_2(H_2L6)_3]^{4+}$ was described. The $H_2L6$ ligand (Figure 5.1) has a flexible biphenyl spacer which allows for the preparation of triple stranded helicates featuring a big cavity. In this chapter, the encapsulation of $[M(III)(ox)_3]^{3-}$ (M = Fe and Cr; ox = oxalate) metal complexes inside the helical cavity of $[Fe_2(H_2L6)_3]^{4+}$ will be described. The Fe(II) atoms of the helicate exhibit SCO behavior and LIESST effect in the case of the encapsulated chromium oxalate complex. Interestingly, the guest $[Cr(III)(ox)_3]^{3-}$exhibits SIM-like behavior at

low temperatures. This is the first example where a host-guest system exhibits both LIESST effect and SIM behavior. In the only related examples, the same Fe(II) ionic species undergoes a photo-induced LS to HS transition and, with continuous light irradiation, the Fe(II) displays also slow relaxation of magnetization.[10,11]

## 5.2 Synthesis and Crystal Structure of $Fe(C_2O_4)_3\subset[Fe_2(H_2L6)_3](BF_4)\cdot 4CH_3OH\cdot 3.7H_2O$ (10)

Complex **10** was prepared from the reaction of $H_2L6$ and $Fe(BF_4)_2.6H_2O$ (1:2 stoichiometry) in $CH_3OH$ at room temperature for 1 hour in the presence of ascorbic acid. The resulting red solution was combined with acetonitrile and left for slow evaporation. The compound was isolated as red single crystals after two weeks. The in situ oxidation of part of the iron ions with oxygen in the presence of ascorbic acid leads to the formation of trisoxalatoferrate(III) $[Fe(C_2O_4)_3]^{3-}$. This anionic ferrioxalate complex is then encapsulated inside the helical cavity (see below).

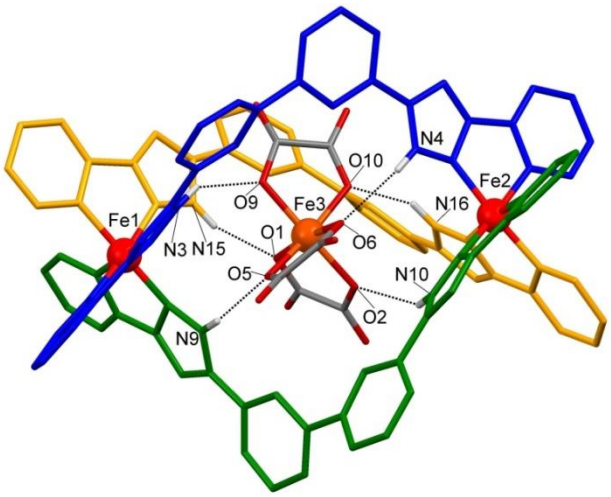


**Figure 5.2**: Molecular representation of $\{Fe(C_2O_4)_3\subset[Fe_2(H_2L6)_3]\}^+$ cation in **10** showing the hydrogen bonding between the NH groups and the oxygen of the oxalate. $BF_4^-$ ion and solvent molecules are omitted for clarity. Only the hydrogen atoms on the pyrazole nitrogen atoms are shown. Only metals and heteroatoms involved in hydrogen bonding are labeled. Fe(II) and Fe(III) are shown in red and orange, respectively.

Complex **10** crystallizes in the triclinic space group *P-1* (*Z*=2). Crystallographic data and selected structural parameters at 100 K are shown in Tables 5.1 and 5.2. The asymmetric unit consists of a cationic $\{Fe(C_2O_4)_3\subset[Fe_2(H_2L6)_3]\}^+$ encapsulating helicate and one $BF_4^-$ counterion in addition to three full $H_2O$ molecules and one $H_2O$

with 70 % partial occupancy. Moreover, four diffused methanol molecules were determined using the PLATON SQUEEZE function[12]. Three $H_2$L6 ligands wrap around the principal axis of the two Fe(II) centers to form a triple-stranded helicate (Figure 5.2). Both Fe(II) centers exhibit a pseudo-octahedral coordination environment arising from three pyrazolylpyridine chelating groups. As the ligands have *C2*-symmetry, the resulting helicate has $D_3$-symmetry. It has a $C_3$ axis which is coincident with the Fe···Fe helical axis and three $C_2$ axes which are perpendicular to the helical axis.

To achieve the helical arrangements, the biphenyl group exhibits a *cis* conformation arising from the appropriate twisting around the central C-C bond. The three ligands exhibit a similar torsion angle between the two phenyl rings in the biphenyl group (average angle of 36.83°). Moreover, the pyrazolylpyridine moiety in each side of the ligand is twisted by an average angle of 14.34 or 21.62° with respect to the adjacent phenyl group. On the other hand, the pyrazole and the pyridine rings are almost within the same plane with twisting angles less than 10°.

The two iron centers are separated by a distance of 10.607 Å. This Fe1···Fe2 distance is only 0.876 Å larger than the one seen in the helical structure in compound **1** (using the ligand $H_2$L4). However, the cavity volume in **10** is 98 $Å^3$ as calculated using Swiss-Pdb Viewer 4.1 (Figure 5.3), which is three and half times larger than the cavity in **1**. The flexible nature of the biphenyl group is the main reason of such big cavity in dinuclear triple-stranded helicate. The trisoxalatoferrate(III) $[Fe(C_2O_4)_3]^{3-}$ metal complex is encapsulated inside the helical cavity and part of the oxalate groups are located between the helical strands (Figure 5.2). Only the Fe(III) center and the six oxygen atoms coordinated to it are located inside the cavity while the rest of each oxalate (two carbon and two oxygen atoms) are located in the large spaces between every two ligand strands. This can be better illustrated by measuring the molecular volume of $[Fe(C_2O_4)_3]^{3-}$ metal complex which is around 183 $Å^3$. This volume is much larger than the volume of the helical cavity. However, the molecular volume of the Fe(III) and the six coordinated oxygen is only 83 $Å^3$, which perfectly fits the cavity volume. The remaining of each oxalate molecule occupies ca. 33 $Å^3$, which fits easily in the large space between the ligand strands.

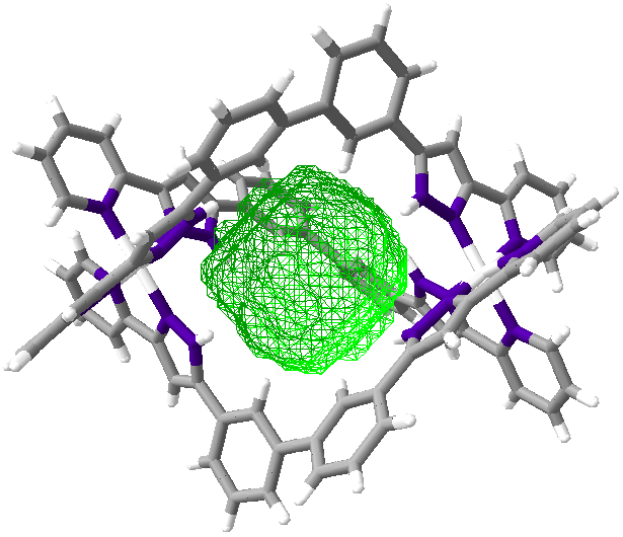

**Figure 5.3**: The crystal structure of **10** with the anions removed and with the volume of the central cavity highlighted as green surface using Swiss-Pdb Viewer 4.1 (Cavity Volume = 98 $Å^3$). In the case of **11**, the volume of the cavity is 92 $Å^3$.

**Table 5.1**: Crystallographic data and selected structural parameters for **10** and **11**.

| Compound | **10** | **11** |
|---|---|---|
| Formula | $Fe_2C_{84}H_{60}N_{18}$,$FeC_6O_{12}$,$BF_4$, 3.7($H_2O$), 4($CH_4O$) | $Fe_2C_{84}H_{60}N_{18}$,$CrC_6O_{12}$,$BF_4$, 6($H_2O$), 1.4($CH_4O$) |
| $M_r$ | 2034.74 | 1980.02 |
| wavelength | 0.77490 | 0.77490 |
| *T* (K) | 100 | 100 |
| Crystal system | Triclinic | Monoclinic |
| Space group | *P-1* | $P2_1/c$ |
| *Z* | 2 | 4 |
| *a* [Å] | 14.757(2) | 19.4808(6) |
| *b* [Å] | 18.198(2) | 16.5141(5) |
| *c* [Å] | 18.783(2) | 28.6823(9) |
| $\alpha$ [º] | 76.047(7) | 90 |
| $\beta$ [º] | 85.146(7) | 109.611(2) |
| $\gamma$ [º] | 79.491(7) | 90 |
| *V* [$Å^3$] | 4808.8(10) | 8692.1(5) |
| $\rho_{calc}$ ($gcm^{-3}$) | 1.405 | 1.520 |
| $\mu$($mm^{-1}$) | 0.624 | 0.685 |
| Independent reflections | 10000 | 14.878 |
| Restraints / parameters | 493/1189 | 22/1281 |
| Goodness of fit on $F^2$ | 1.145 | 1.031 |
| Final $R_1$/$wR_2$ [I>2σ(I)] | 0.1242/0.3375 | 0.0488/0.1254 |
| Final $R_1$/$wR_2$ [all data] | 0.1660/0.3631 | 0.0730/0.1394 |
| Largest diff. peak and hole (e$Å^3$) | 3.560/-0.669 | 1.199/-0.727 |

**Table 5.2**: Selected interatomic distances [Å] and selected structural factors found in **10**.

| | | | |
|---|---|---|---|
| Fe1-N1 | 1.98(1) | Fe2-N5 | 1.962(8) |
| Fe1-N2 | 1.93(1) | Fe2-N6 | 2.00(1) |
| Fe1-N7 | 1.99(1) | Fe2-N11 | 1.92(1) |
| Fe1-N8 | 1.930(9) | Fe2-N12 | 1.96(1) |
| Fe1-N13 | 1.994(8) | Fe2-N17 | 1.94(1) |
| Fe1-N14 | 1.939(9) | Fe2-N18 | 1.983(8) |
| | | | |
| Fe1⋯Fe2 | 10.607(3) | Fe1⋯Fe3 | 5.283(2) |
| Fe2⋯Fe3 | 5.323(2) | N3-H⋯O9 | 2.186 |
| N4-H⋯O6 | 2.237 | N9-H⋯O5 | 2.089 |
| N10-H⋯O2 | 2.355 | N15-H⋯O1 | 2.166 |
| N16-H⋯O10 | 2.107 | O1W⋯H-N10 | 2.29 |
| O1W⋯O4 | 2.61(2) | O2W⋯H-N3 | 2.53 |
| O2W⋯O11 | 2.65(2) | O3W⋯H-N4 | 2.52 |
| O3W⋯O8 | 2.56(2) | O4W⋯H-N15 | 2.53 |
| O4W⋯O3 | 2.40(3) | | |
| | | | |
| $(Fe\text{-}N)_{avg}$ [a] | 1.961/1.959 | $\Sigma(^\circ)$ [a] | 69.76/64.69 |
| $\Theta(^\circ)$ [a] | 213.3/202.0 | $V_{oct}$ [a] | 9.85/9.84 |
| *S(Oh)* [a] | 0.7738/0.7315 | *S(itp)* [a] | 15.0528/14.7218 |

a: In Fe1/Fe2 form

The ferrioxalate guest could be present in $\Delta$ or $\Lambda$ enantiomer. Therefore, in every discrete encapsulated helicate the two Fe(II) and the Fe(III) ions have the same chirality such that each individual complex is either $\Delta\Delta\Delta$(*P*) or $\Lambda\Lambda\Lambda$(*M*) leading to a racemic mixture of the two enantiomers within the lattice

Fe(III) of the ferrioxalate guest locates on the principal helical axis and almost mid way between the external Fe(II) centers [Fe1⋯Fe3 = 5.283 and Fe2⋯Fe3 = 5.323 ˚Å]. The inclusion of the ferrioxalate complex inside the helical cavity is mainly stabilized by six strong hydrogen bonds formed between the coordinated oxygen of the oxalate and the N-H groups of the pyrazole moiety (N-H⋯O distances in the range 2.089-2.237Å, see Table 5.2).

At look, the Fe-N distances involving the pyridine nitrogen atoms are slightly longer than those engaging the pyrazole ring. However, average distances of 1.961 Å and 1.959 Å were found for (Fe1-N) and (Fe2-N), respectively. This indicates a low spin configuration for both Fe(II) centers in agreement with bulk magnetic studies (see below). Moreover, the distortion parameters $\Sigma$ and $\Theta$, and the continuous symmetry measures [*S(Oh)* and *S(itp)*] (Table 5.2) for both iron centers are similar to these seen

for LS Fe(II) centers in the previous helicates (chapter 3). The average Fe3-O distances in the ferrioxalate groups is 2.006 Å which is similar to the average value observed in the crystal structure of $K_{2.9}Na_{0.1}Fe(C_2O_4)_3\ 3H_2O$ (2.009 Å).[13]

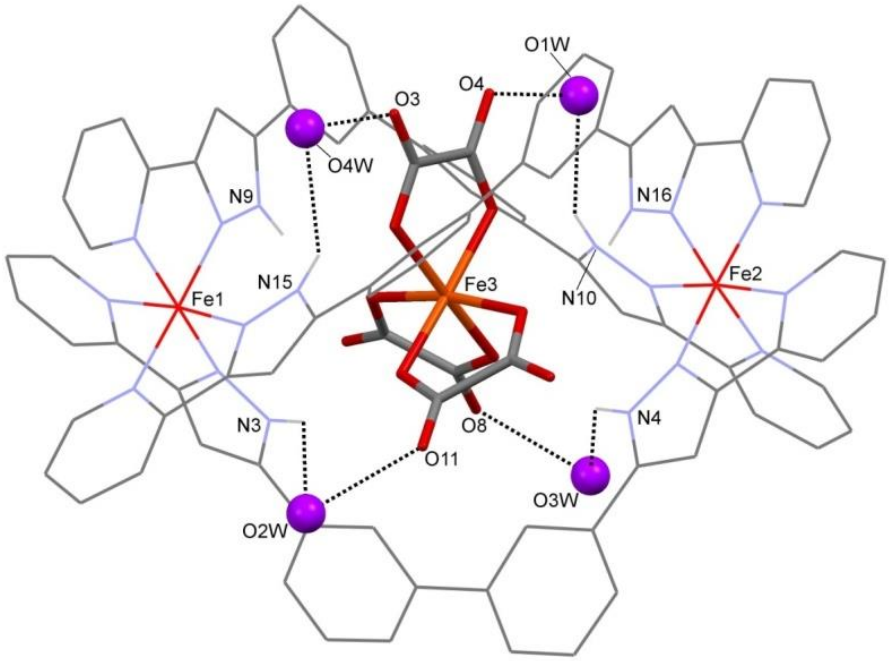


**Figure 5.4**: Molecular representation of $\{Fe(C_2O_4)_3 \subset [Fe_2(H_2L6)_3]\}^+$ cation in **10** showing the hydrogen bonding between the NH groups or the non-coordinated oxygen of the oxalate in one side with the water molecules. Only the hydrogen atoms on the pyrazole nitrogen atoms are shown. Only metals and heteroatoms involved in hydrogen bonding are labeled. Helicate, guest and water molecules are shown in different style for clarity. Water molecules are shown in violet.

The four water molecules are located close to the helical structure and they are involved in strong hydrogen bonds with the N-H groups and the non-coordinated oxygen of the oxalate moieties (Figure 5.4). The OW···H-N and OW···$O_{ox}$ intermolecular distances are in the range 2.294-2.648 Å (Table 5.2). Three of these water molecules interact with oxalates from two different guests (Figure 5.5). Thus, two water molecules bridge two oxalate complexes in *anti-anti* fashion by making hydrogen bonds with one non-coordinated oxygen atom in each oxalate. As a result, the crystal packing consists of a 2*D* network in the *cb* plane formed by the supramolecular interaction between oxalates and the water solvent molecules (Figure 5.5). Moreover, the helicates interact together through weak $\pi$-$\pi$ interactions between their aromatic rings along the same plane of the

2*D* supramolecular network. As seen in Figure 5.6, the host $[Fe_2(H_2L6)_3]^{4+}$ helicates are interacting with their neighbors through their biphenyl and pyridine groups.

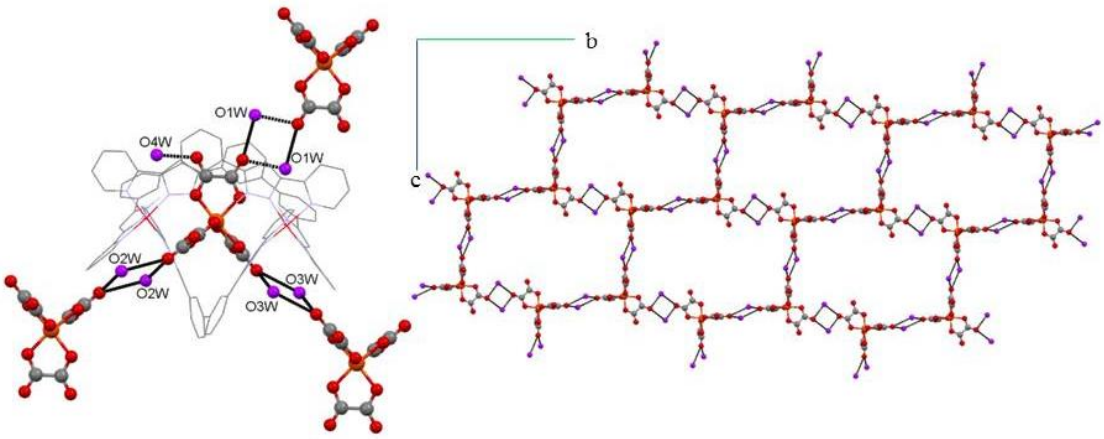


**Figure 5.5**: Representation of the supramolecular bridging in **10** of the central ferrioxalate guest with the first three neighbors via water molecules (left) to form a 2*D* packing network (right).The helicates of the neighbor molecules and the helicates of the 2*D* network are not shown for clarity. Water molecules are shown in violet. O4W participate in hydrogen bond with only one oxalate and thus is not shown in the 2*D* network representation.

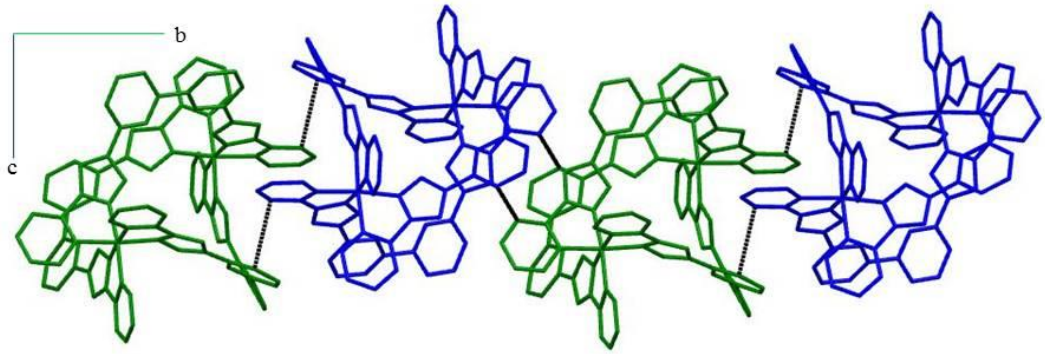


**Figure 5.6**: Representation of the interaction between alternative helicates $[Fe_2(H_2L6)_3]^{4+}$ of **10** in the same plane of the 2*D* supramolecular network showing the $\pi$-$\pi$ interactions formed between them as shortest C···C contacts between the concerned rings..

## 5.3 Magnetic Properties of $Fe(C_2O_4)_3 \subset [Fe_2(H_2L6)_3](BF_4)\cdot 4CH_3OH\cdot 3.7H_2O$ (10)

Magnetic susceptibility measurements on compound **10** were carried out using a polycrystalline sample in the temperature range 2-320 K under constant magnetic field

of 0.5 T. The plot of $\chi_m T$ *vs. T* and the field dependence of the magnetization measured at three different temperatures are shown in Figure 5.7. In the range10-100 K, $\chi_m T$ shows a plateau at 3.90 $cm^3mol^{-1}K$, which indicates the presence of one HS Fe(III) ($g$ = 1.90) and two LS Fe(II) centers in agreement with the crystal structure at 100 K. Below 10 K, the decline in $\chi_m T$ down to 3.59 $cm^3mol^{-1}K$ is due to ZFS of the Fe(III) centers. The $\chi_m T$ value starts to increase very gradually above 100 K reaching a maximum value of 5.19 $cm^3mol^{-1}K$ at 320 K. This value corresponds to a HS⇔LS conversion of the Fe(II) centers of ca. 54%. This gradual SCO is not complete at the maximum temperature reachable by the SQUID magnetometer.

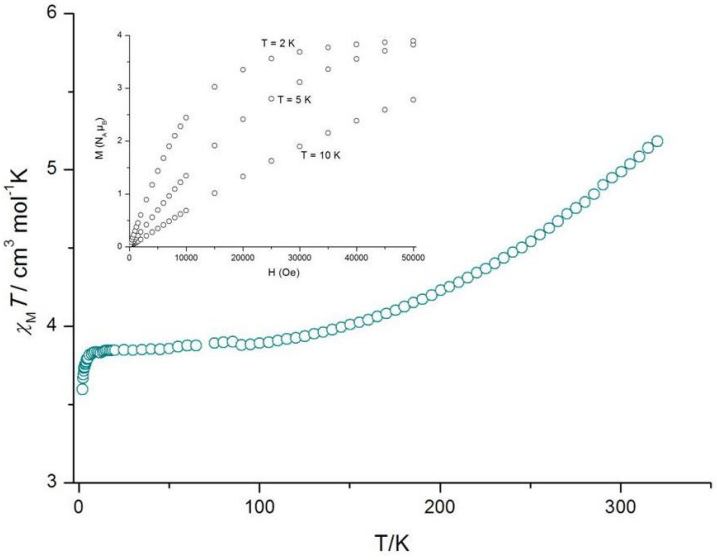


**Figure 5.7**: Temperature dependence of $\chi_m T$ in **10**. Inset: Field dependence of the magnetization at three different temperatures.

## 5.4 Mass Spectrometry of $Fe(C_2O_4)_3 \subset [Fe_2(H_2L6)_3](BF_4)\cdot 4CH_3OH\cdot 3.7H_2O$ (10)

Due to the low solubility of **10** in common solvents, mass spectrometry experiments were conducted by dissolving the solid in DMSO followed by dilution with $CH_3OH$ using the positive ion electrospray ($ESI^+$) technique.

The results indicate the stability of the encapsulated helicate in solution (Figure 5.8). A peak of the encapsulated-helicate $\{Fe(C_2O_4)_3 \subset [Fe_2(H_2L6)_3]\}^+$was detected at m/z = 1753.28. This peak corresponds to the cation observed in the solid state with the $Fe(C_2O_4)_3^{3-}$ found inside the helical cavity. Moreover, a peak with 2+ charge was observed at m/z = 876.64 which corresponds to the same helicate with an additional

proton;$\{Fe(C_2O_4)_3\subset[Fe_2(H_2L6)_3)] + H\}^{2+}$. The isotopic distribution of the peak is consistent with the one theoretically expected as shown in Figure 5.9.

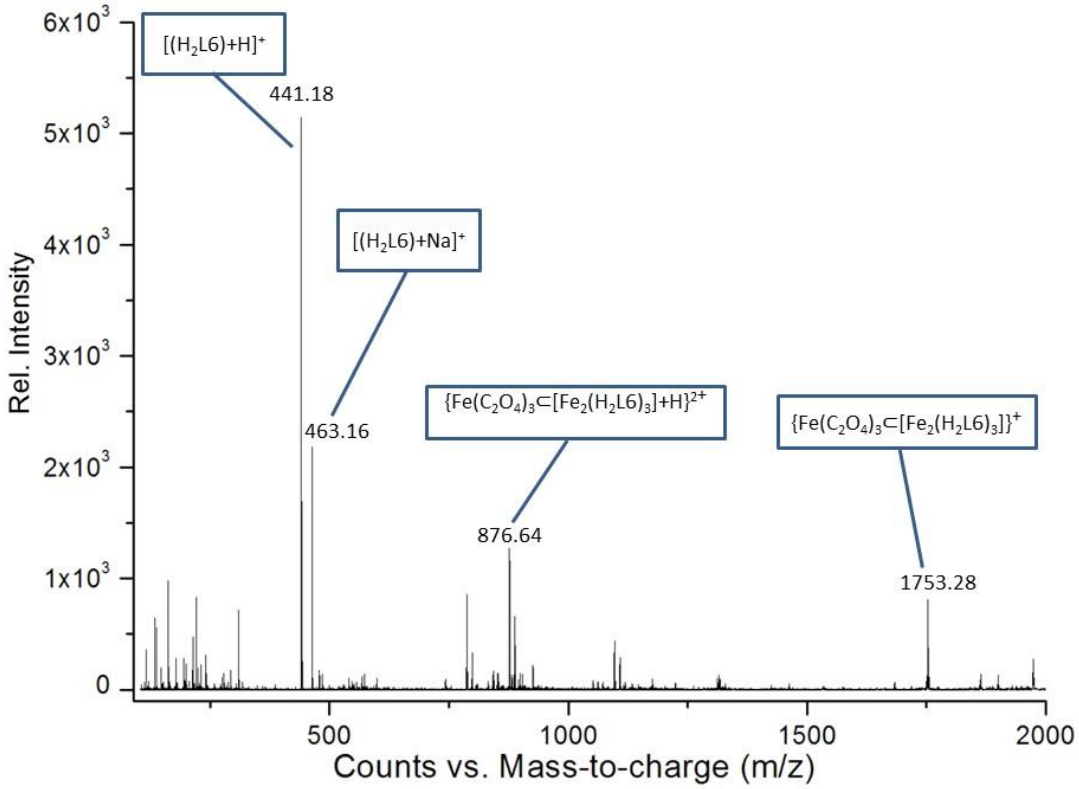


**Figure 5.8**: Mass spectrum of **10** in DMSO-MeOH mixture with identification of the important peaks.

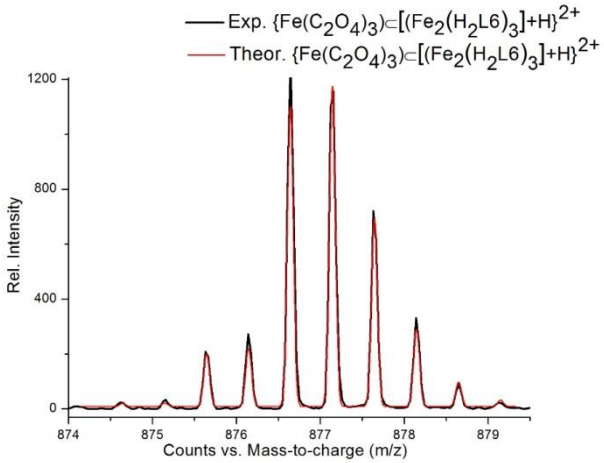


**Figure 5.9**: The match of theoretical and experimental isotopic distribution of the encapsulated helicate peaks$\{Fe(C_2O_4)_3\subset[Fe_2(H_2L6)_3)] + H\}^{2+}$ in **10**.

## 5.5 Synthesis and Crystal Structure of $Cr(C_2O_4)_3 \subset [Fe_2(H_2L6)_3](BF_4)\cdot 1.4CH_3OH\cdot 6H_2O$ (11)

Compound **11** was prepared by layering two solutions; an aqueous solution of $K_3[Cr(C_2O_4)_3].3H_2O$ and a methanolic solution resulting from the reaction of $Fe(BF_4)_2$ with $H_2L6$. Red-orange crystals suitable for X-ray structure determination were collected after two weeks. Smaller crystals in higher yield could be obtained after seven days by combining the second solution with a solution of $K_3[Cr(C_2O_4)_3].3H_2O$ in minimum amount of 1:1 $CH_3OH$-$H_2O$ mixture.

**Table 5.3**: Selected interatomic distances [Å] and structural factors found in **11.**.

| | | | |
|---|---|---|---|
| Fe1-N1 | 1.973(3) | Fe2-N5 | 1.964(3) |
| Fe1-N2 | 1.931(3) | Fe2-N6 | 1.996(3) |
| Fe1-N7 | 1.964(3) | Fe2-N11 | 1.970(3) |
| Fe1-N8 | 1.943(3) | Fe2-N12 | 1.994(3) |
| Fe1-N13 | 1.996(3) | Fe2-N17 | 1.956(3) |
| Fe1-N14 | 1.957(3) | Fe2-N18 | 2.007(3) |
| | | | |
| Fe1⋯Fe2 | 10.6824(8) | Fe1⋯Cr1 | 5.4126(7) |
| Fe2⋯Cr1 | 5.2710(7) | N3-H⋯O1 | 2.71(4) |
| N4-H⋯O10 | 1.94(3) | N9-H⋯O5 | 2.08(3) |
| N10-H⋯O2 | 1.92(3) | N15-H⋯O9 | 2.21(3) |
| N16-H⋯O6 | 2.07(3) | O1W⋯O3 | 2.755(4) |
| O7W⋯O7 | 2.72(1) | O3W⋯O4 | 3.014(5) |
| O6W⋯O5W | 2.847(9) | O11⋯O5W | 2.825(6) |
| O6W⋯O12 | 2.780(9) | O6W⋯O12 | 2.780(9) |
| | | | |
| $(Fe\text{-}N)_{avg}$[a] | 1.961/1.981 | $\Sigma(^\circ)$[a] | 62.4/63.4 |
| $\Theta(^\circ)$[a] | 189.5/195.1 | $V_{oct}$ (Å$^3$)[a] | 9.88/10.18 |
| *S(Oh)*[a] | 0.671/0.757 | *S(itp)*[a] | 14.729/13.966 |

a: In Fe1/Fe2 form

**Table 5.4**: Crystallographic data for **11** at eight different temperatures.

| Formula | $Fe_2C_{84}H_{60}N_{18}$,$CrC_6O_{12}$,$BF_4$, 6($H_2O$), 2($CH_4O$) | | | | | | | $Fe_2C_{84}H_{60}N_{18}$,$CrC_6O_{12}$,$BF_4$, 3.6($H_2O$), 0.7($CH_4O$) |
|---|---|---|---|---|---|---|---|---|
| FW (g $mol^{-1}$) | 2008.25 | | | | | | | 1923.32 |
| Wavelength (Å) | 0.77490 | | | | | | | |
| Crystal system | Tetragonal | | | | | | | |
| Space group | $I4_1cd$ | | | | | | | |
| *Z* | 16 | | | | | | | |
| *T* (K) | 90(2) | 100(2) | 130(2) | 160(2) | 190(2) | 220(2) | 250(2) | 280(2) |
| *a* (Å) | 19.597(1) | 19.6011(13) | 19.654(1) | 19.694(1) | 19.799(1) | 19.944(1) | 20.032(1) | 20.161(2) |
| *b*(Å) | 16.5472(9) | 16.5502(10) | 16.582(1) | 16.6182(9) | 16.6609(9) | 16.691(1) | 16.712(1) | 16.423(2) |
| *c* (Å) | 28.766(2) | 28.767(2) | 28.778(2) | 28.786(2) | 28.789(2) | 28.753(2) | 28.781(2) | 28.633(3) |
| *V* ($Å^3$) | 8769.2(9) | 8774.9(10) | 8807.9(9) | 8837.9(9) | 8887.6(9) | 8935.4(10) | 8971.5(10) | 8816.1(17) |
| $\rho_{calcd}$ (g $cm^{-3}$) | 1.521 | 1.520 | 1.514 | 1.509 | 1.501 | 1.486 | 1.487 | 1.449 |
| $\mu$ ($mm^{-1}$) | 0.680 | 0.680 | 0.677 | 0.675 | 0.671 | 0.667 | 0.665 | 0.647 |
| Independent reflections | 9242 | 12156 | 9282 | 9341 | 9385 | 9538 | 9491 | 6558 |
| restraints / parameters | 77/1255 | 71/ 1255 | 105/ 1225 | 107/ 1220 | 138/ 1205 | 136/ 1204 | 131/1203 | 1288 /1173 |
| Goodness-of-fit on $F^2$ | 1.058 | 1.059 | 1.067 | 1.059 | 1.078 | 1.062 | 1.071 | 1.084 |
| Final $R_1$ / w$R_2$ | 0.1121/ | 0.1217/ | 0.1156/ | 0.1099/ | 0.1143/ | 0.1294/ | 0.1234/ | 0.1596/ |
| [$I>2\sigma(I)$] | 0.3201 | 0.3511 | 0.3362 | 0.3184 | 0.3314 | 0.3662 | 0.3806 | 0.4244 |
| Final $R_1$ / w$R_2$ | 0.1421/ | 0.1560/ | 0.1471/ | 0.1414/ | 0.1492/ | 0.1722/ | 0.1627/ | 0.2235/ |
| [all data] | 0.3478 | 0.3817 | 0.3677 | 0.3509 | 0.3659 | 0.4047 | 0.3866 | 0.4833 |
| largest diff. peak and hole (*e* $Å^3$) | 1.313/ -0.699 | 1.475/ -0.815 | 0.1305/ -0.767 | 1.160/ -0.762 | 1.058/ -0.818 | 1.336/ -0.738 | 1.359/ -0.647 | 1.058/ -1.026 |

**Table 5.5**: Selected interatomic distances [Å] and structural parameters found in **11** at eight different temperatures.

| *T* (K) | 90(2) | 100(2) | 130(2) | 160(2) | 190(2) | 220(2) | 250(2) | 280(2) |
|---|---|---|---|---|---|---|---|---|
| Fe1–N14 | 1.95(1) | 1.948(9) | 1.96(1) | 1.95(1) | 1.96(1) | 1.94(1) | 1.95(1) | 1.96(2) |
| Fe1–N8 | 1.95(1) | 1.95(1) | 1.95(1) | 1.95(1) | 1.94(1) | 1.95(2) | 1.94(1) | 1.94(3) |
| Fe1–N2 | 1.93(1) | 1.94(1) | 1.93(1) | 1.93(1) | 1.93(1) | 1.93(1) | 1.94(1) | 1.94(2) |
| Fe1–N1 | 1.98(1) | 1.98(1) | 1.98(1) | 1.99(1) | 2.00(1) | 2.00(2) | 2.00(1) | 2.02(3) |
| Fe1–N13 | 1.98(1) | 1.98(1) | 1.98(1) | 1.98(1) | 1.99(1) | 1.98(1) | 1.99(1) | 1.96(2) |
| Fe1–N7 | 1.96(1) | 1.958(9) | 1.96(1) | 1.97(1) | 1.97(1) | 1.97(1) | 1.97(1) | 1.99(2) |
| Fe2–N17 | 1.96(1) | 1.95(1) | 1.96(1) | 1.98(1) | 2.00(1) | 2.05(2) | 2.08(2) | 2.13(3) |
| Fe2–N5 | 1.95(1) | 1.951(9) | 1.95(1) | 1.97(1) | 1.99(1) | 2.02(1) | 2.04(1) | 2.09(2) |
| Fe2–N11 | 1.96(1) | 1.96(1) | 1.96(1) | 1.96(1) | 1.98(1) | 2.01(1) | 2.04(1) | 2.07(3) |
| Fe2–N18 | 2.01(1) | 2.00(1) | 2.01(1) | 2.03(1) | 2.05(1) | 2.07(2) | 2.10(2) | 2.14(3) |
| Fe2–N6 | 2.02(1) | 2.01(1) | 2.03(1) | 2.04(1) | 2.06(1) | 2.11(2) | 2.16(2) | 2.22(3) |
| Fe2–N12 | 1.99(1) | 2.00(1) | 2.00(1) | 2.00(1) | 2.04(1) | 2.06(2) | 2.11(2) | 2.14(3) |
| <Fe1–N> | 1.955 | 1.954 | 1.960 | 1.960 | 1.965 | 1.960 | 1.960 | 1.960 |
| <Fe2–N> | 1.975 | 1.980 | 1.980 | 1.990 | 2.020 | 2.055 | 2.090 | 2.135 |
| Fe1···Fe2 | 10.706(3) | 10.712(2) | 10.702(3) | 10.700(2) | 10.687(3) | 10.669(3) | 10.652(3) | 10.609(5) |
| $\Sigma$ (°)[a] | 60.9/60.1 | 59.8/61.7 | 59.6/60.8 | 60.0/62.7 | 62.0/67.5 | 60.6/69.5 | 62.0/76.8 | 57.0/88.0 |
| $\Theta$ (°)[a] | 186.9/194.1 | 184.2/198.4 | 186.3/195.2 | 187.5/201.3 | 190.0/217.2 | 188.3/221.0 | 191.3/241.2 | 184.1/274.2 |
| *S(Oh)*[a] | 0.657/0.742 | 0.645/0.769 | 0.656/0.748 | 0.667/0.800 | 0.686/0.939 | 0.662/1.016 | 0.692/1.231 | 0.676/1.654 |
| *S(itp)*[a] | 14.587/14.065 | 14.534/14.021 | 14.453/14.073 | 14.368/13.889 | 14.473/13.538 | 14.508/13.068 | 14.358/12.585 | 14.308/11.693 |
| $V_{oct}$ (Å$^3$)[a] | 9.86/10.18 | 9.87/10.15 | 9.89/10.23 | 9.91/10.41 | 9.95/10.73 | 9.92/11.28 | 9.93/11.83 | 10.00/12.50 |

a) In Fe1/Fe2 form.

Compound **11** crystallizes in the monoclinic space group $P2_1/c$ ($Z$ = 4). Crystal data and selected structural parameters at 100 K are shown in Tables 5.1 and 5.3. The asymmetric unit includes the encapsulating helicate $\{Cr(C_2O_4)_3 \subset [Fe_2(H_2L6)_3]\}^+$ in addition to a $BF_4^-$ counter ion, six water molecules, one methanol molecule and another methanol molecule with 0.4 occupancy. Similar to **10**, the triple stranded helicate encapsulates the $[Cr(C_2O_4)_3]^{3+}$ metal complex in the central cavity. The volume of the cavity (92 $Å^3$) is slightly smaller than that seen in **10** as calculated using Swiss-Pdb Viewer 4.1 (Figure 5.3). However, the intrahelical distance Fe1···Fe2 is 10.682 Å which is slightly longer than that seen in **10**. The $Cr^{3+}$ ion locates closer to Fe2 by 0.142 Å [Fe1···Cr1 = 5.413 and Fe2···Cr1 = 5.271 Å]. Again, a racemic mixture of two enantiomers *ΔΔΔ* (*P*) or *ΛΛΛ* (*M*) of the encapsulated helicate is present in the crystal.

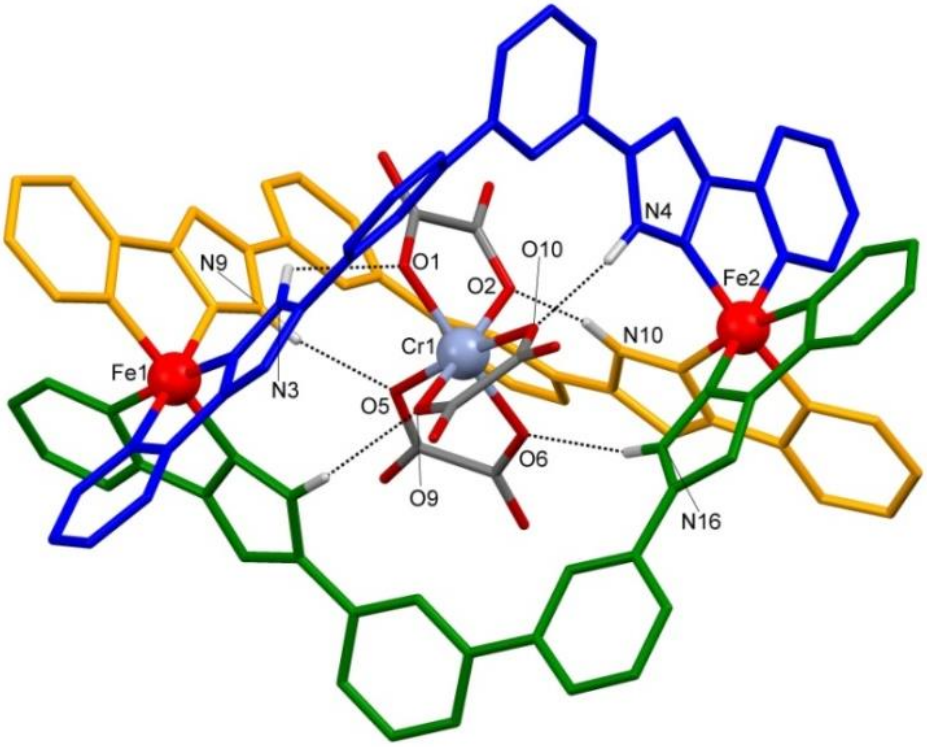


**Figure 5.10**: Molecular representation of the cationic encapsulated helicate $\{Cr(C_2O_4)_3 \subset [Fe_2(H_2L6)_3]\}^+$ in **11** showing the hydrogen bonding between the NH groups and the oxygen of the oxalate. $BF_4^-$ ion and solvent molecules are omitted for clarity. Only the hydrogen atoms on the pyrazole nitrogen atoms are shown. Only metals and heteroatoms involved in hydrogen bonding are labeled.

The coordinated oxygen atoms of the guest $[Cr(C_2O_4)_3]^{3+}$ are involved in strong hydrogen bonds with the N-H groups, with N-H···O distances that fall in the range

1.92-2.71 Å (Table 5.3). The contacts lying closer to Fe2 are much stronger than the others, thus making the oxalate complex to be closer to this Fe(II) center. The Fe-$N_{avg}$ values are 1.961 and 1.981Å for Fe1 and Fe2, respectively, indicating a LS state at 100 K in agreement with bulk magnetic studies. The Cr-$O_{avg}$ in the oxalate complex is 1.973 Å, which is similar to that seen in the crystal structure of $K_3[Cr(C_2O_4)_3].3H_2O$ (1.969 Å).[14]

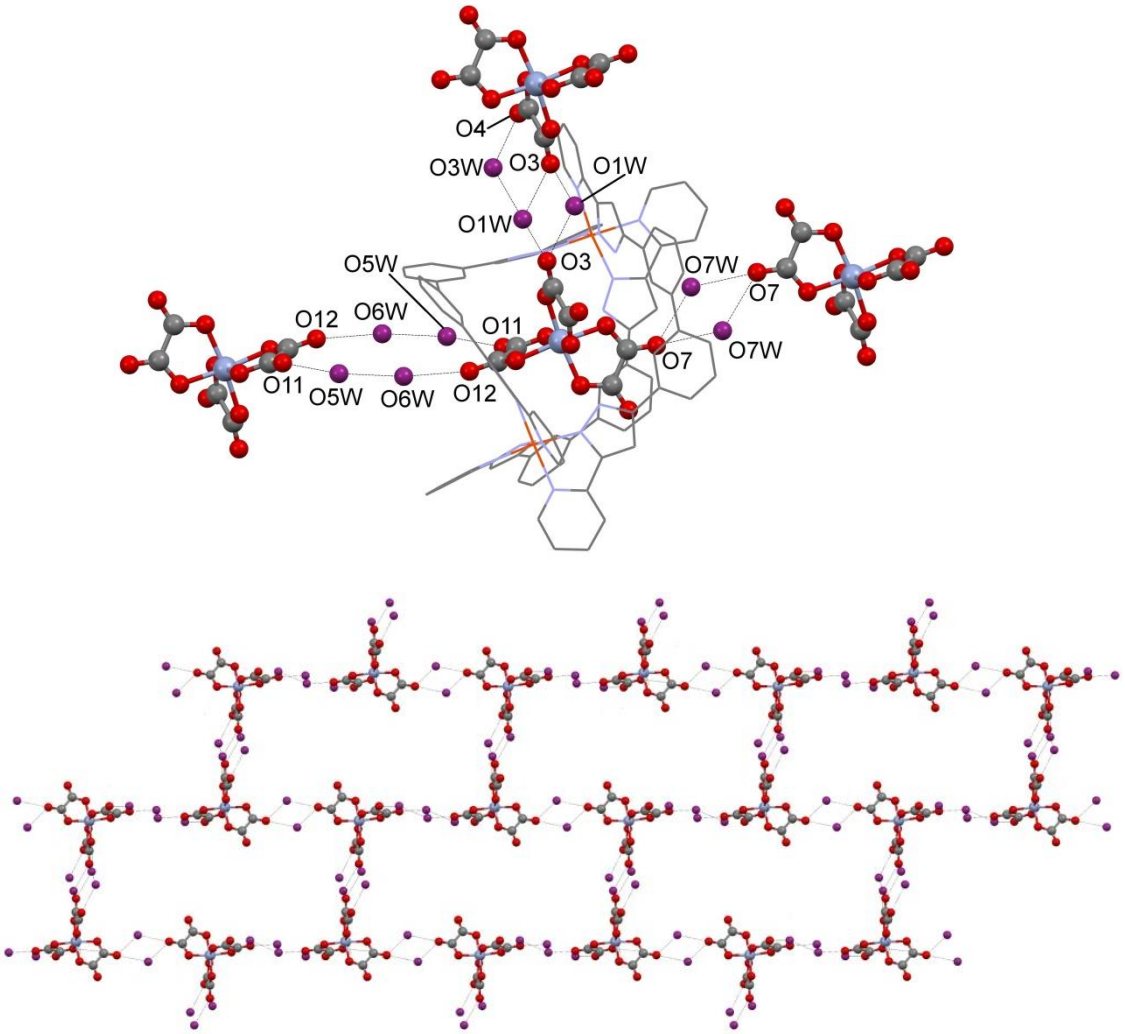


**Figure 5.11**: Representation of the supramolecular bridging in **11** of the central $Cr(ox)_3^{3-}$ guest with the first three neighbors via water molecules (top) to form a 2*D* packing network (bottom). The helicates of the neighbor molecules and the helicates in the 2*D* network are not shown for clarity. Water molecules are shown in violet. Some water molecules do not participate in the bridging between the oxalate ions and they are not shown for clarity.

The six water molecules are participating in hydrogen bonding interactions with the oxalate ions and with each other. These strong interactions yield a 2*D* packing network

of the $\{Cr(C_2O_4)_3 \subset [Fe_2(H_2L6)_3]\}^+$ helicates (Figure 5.11). Some water molecules and methanol molecules do not interact directly with oxalate and just interact with other water molecules. The helicates interact together through weak $\pi$-$\pi$ interactions between aromatic rings along the same plane of the 2*D* supramolecular network, similar to what is seen in Figure 5.6 for compound **10.**

Variable temperature crystallographic studies were conducted at eight different temperatures on one crystal in order to investigate the variations of the magnetic state of the iron centers (Tables 5.4 and 5.5). The plot of Fe-$N_{avg}$ vs. temperature for both iron centers indicates that the spin state of Fe2 changes from LS to HS state (Fe2-$N_{avg}$ changes from around 1.980 Å below 160 K to 2.135 Å at 280 K) while Fe1 remains in the LS state (Fe1-$N_{avg}$ is almost constant around 1.960 Å) in the same range of temperatures. The Spin crossover for Fe2 is not complete at 280 K and corresponds to around 85 % of conversion to HS. This agrees with the magnetic studies, which show a SCO corresponding to one iron center with $T_{1/2}$ around 240 K (see below). The crystal loses some of the solvents through heating above 250 K, but the magnetic properties do not seem affected by these changes. This is because molecules that evacuate the lattice upon heating are not directly interacting with the supramolecular assembly.

In addition, the change in the octahedral geometry [measured by the distortion parameter $\Sigma$ and $\Theta$ and continuous symmetry measures {*S(Oh)* and *(S(itp)*} (see chapters 1 and 3 for details about these parameters) around both iron centers indicate clearly the SCO in Fe2. As expected, this iron center exhibits significant distortion from octahedral geometry toward trigonal prism as the temperature increases as a result of the LS to HS state transition. In contrast, these parameters do not change significantly for Fe1 since it remains in the LS state.

Plotting the cell parameters with respect to the temperature shows a continuous and gradual change in the range 160-250 K, which could be ascribed to the SCO behavior in addition to the thermal expansion of the lattice. The solvents losses occurring at the highest temperatures (above 250) cause a sudden decrease in these parameters. This makes it difficult to see the effect of SCO at these parameters since the gradual SCO occurs precisely in the range 190-300 K. However, the loss of the solvents does not affect the SCO behavior itself as seen in the bulk magnetic studies.

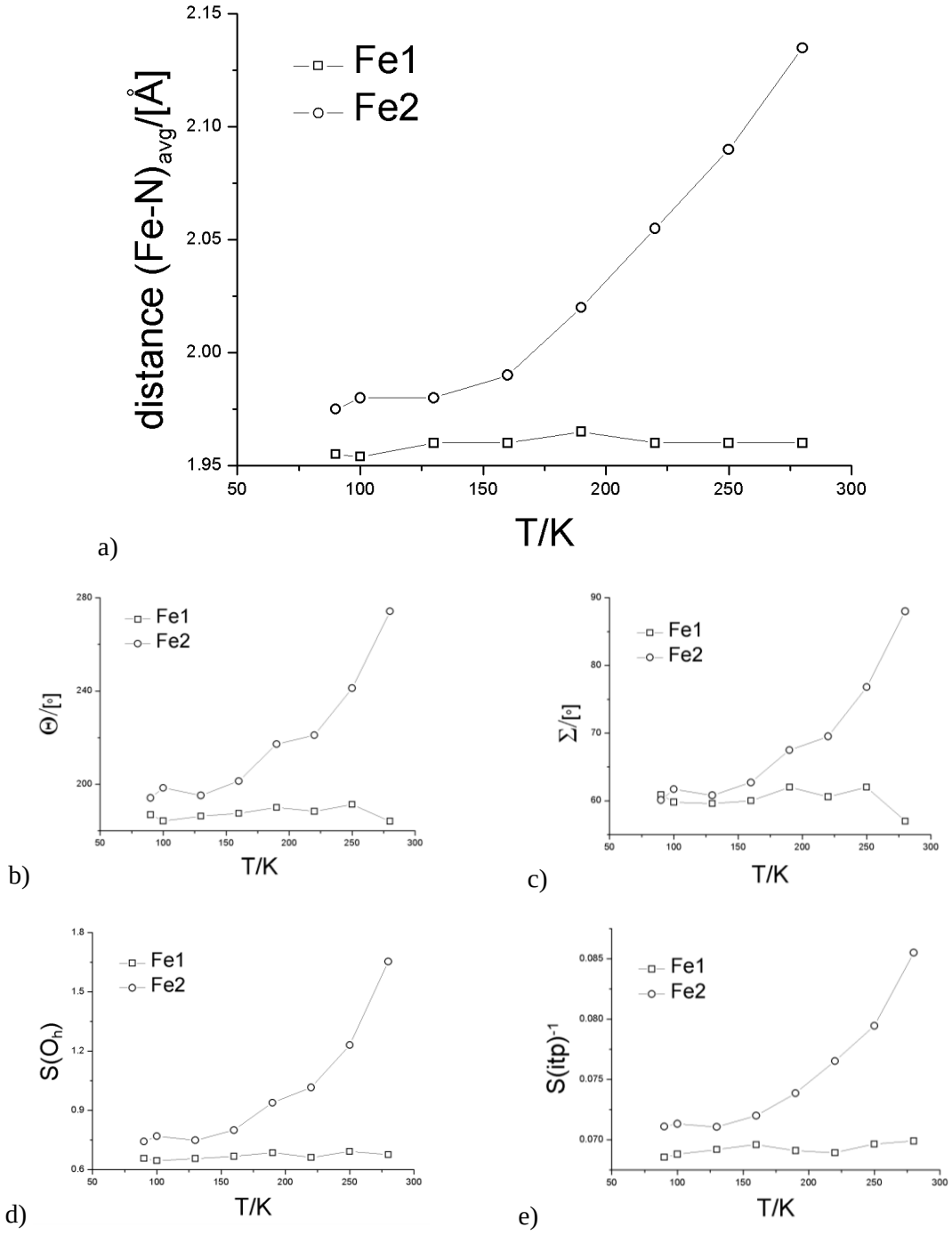


**Figure 5.12**: Temperature dependence of a) Fe-$N_{avg}$, b) $\Sigma$ distortion parameter, c) *S(Oh)* and d) $S(itp)^{-1}$ symmetry measures for both iron centers in **11** as determined from single crystal X-ray diffraction data.

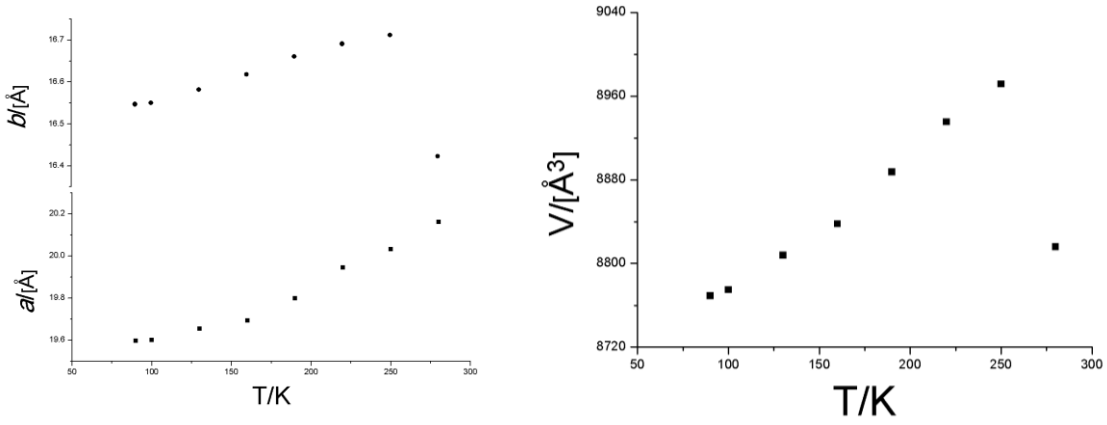


**Figure 5.13**: Plots of cell parameters change (cell lengths *a* and *b* and cell volume) associated with temperature increasing in compounds **11**.

## 5.6 Static Magnetic Properties of $Cr(C_2O_4)_3 \subset [Fe_2(H_2L6)_3](BF_4)\cdot 1.4CH_3OH\cdot 6H_2O$ (11)

Magnetic susceptibility measurements for compound **11** were performed in the temperature range 2-320 K under a constant magnetic field of 0.5 T. The plot of $\chi_m T$ *vs.* *T* and the field dependence of the magnetization are shown in Figure 5.14. The plateau of $\chi_m T$ below 100 K at *ca.* 1.90 $cm^3mol^{-1}K$ is consistent with the presence of two LS Fe(II) centers ($S$ = 0) and one HS Cr(III) ion ($S$ = 3/2, spin-only value of $\chi_m T$ is 1.875 $cm^3mol^{-1}K$) in agreement with the crystal structure at 100 K. The spin-orbit coupling constant in $Cr^{3+}$ is very small and the deviation from the $\chi_m T$ spin-only value is almost negligible.[15] This is supported by the field dependence of the magnetization measured at 2 K, which reaches a quasi saturation value of 2.9 $\mu_B$ ($M_{sat}$ = 3 $N_A\mu_B$ for S = 3/2). The slight decrease of $\chi_m T$ below 10 K is due to ZFS of the Cr(III) ions. The molar magnetic susceptibility below 60 K and the magnetization data at 2 and 5 K were fitted simultaneously in PHI program using the spin Hamiltonian:

$$\hat{H} = \frac{D}{3}\hat{O}_2^0 + E\hat{O}_2^2 + \mu_B g B \hat{S}$$

Where $\hat{O}_2^0$ and $\hat{O}_2^2$ are Stevens operators:

$$\hat{O}_2^0 = 3L_z^2 - L^2$$

$$\hat{O}_2^2 = \frac{1}{2}(L_+^2 - L_-^2)$$

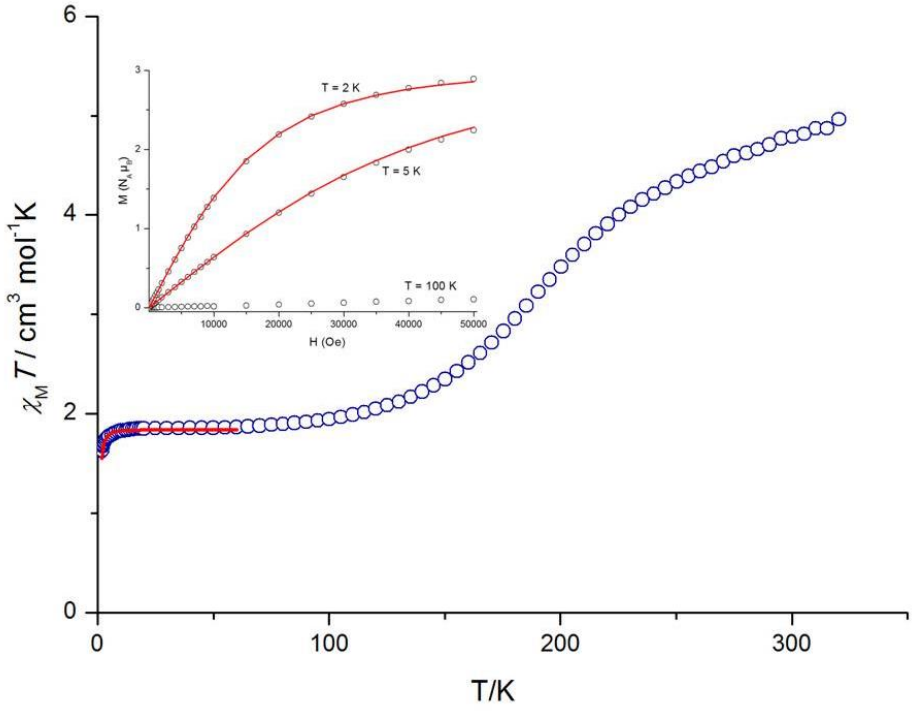


**Figure 5.14**: Temperature dependence of $\chi_m$T in **11**. Inset: Field dependence of the magnetization at three different temperatures. Red lines is the best fit for the experimental data using PHI program yielding average values of $g$ = 1.98, $D$ = 0.622 and $E$ = -0.346.

The best fit for the experimental data yield an average value of $g$ = 1.98, $D$ = 0.622 and $E$ = -0.346 where $D$ and $E$ is the axial and the transverse magnetic anisotropy parameters. The $g$-factor value which is slightly lower than 2.0 and the small and positive ZFS D parameter is consistent with the values seen in hexacoordinated Cr(III) complexes [ex. $Cr(acac)_3$].[15,16] The distortion from octahedral geometry around the $Cr^{3+}$ ion can be quantified using the distortion parameter $\Sigma$ (47.76) and interatomic symmetry measures *S(Oh)* (0.559) which indicates intermediate distortion and agrees with such small $D$ value.

A gradual increase of $\chi_m T$ above 100 K is observed due to SCO of the Fe(II) centers. The maximum $\chi_m T$ value a 315 K is 4.88 $cm^3mol^{-1}K$ which indicates a LS to HS state conversion of 50 % of the Fe(II) ions. This agrees with the crystal structure at 280 K which shows an ordered HS-LS mixed state of the dinuclear helicate (see above). The $T_{1/2}$ of the SCO is approximately 240 K.

## 5.7 Calorimetry Studies of $Cr(C_2O_4)_3 \subset [Fe_2(H_2L6)_3](BF_4)\cdot 1.4CH_3OH\cdot 6H_2O$ (11)

The thermal spin crossover in compound **11** was studied using Differenial Scanning Calorimetry (DSC) measurements. The temperature dependence of the molar heat capacity at constant pressure ($C_p$) is shown in Figure 5.15 (left). A very broad hump was observed in the expected range for the SCO process. This agrees with the gradual character of the SCO as observed during the magnetic studies. Another increase in the $C_p(T)$ was observed above 280 K, which likely corresponds to lattice solvent loss, in agreement with the crystal structure studies at 280 K.

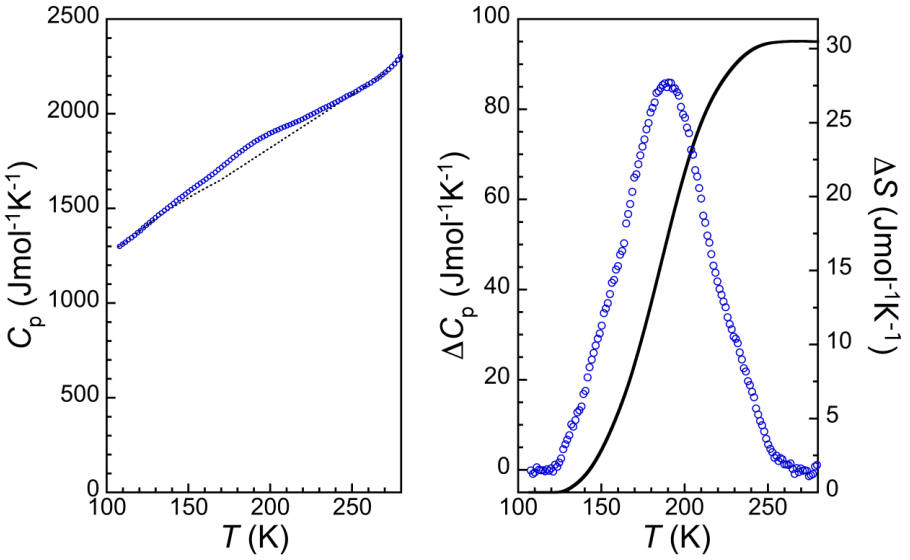


**Figure 5.15**: Molar heat capacity of **11**, showing broad endothermic peak arising from the spin transition. Dotted curve indicates the normal heat capacity. Right) excess heat capacity ($\Delta C_p$) beyond the normal heat capacity as a result of the spin crossover in **11** (open cycles), black solid line: excess entropy involved in SCO behavior as derived from the integration of the $\Delta C_p$ *vs.* *lnT*.

On the basis of the magnetic data, the lattice heat capacity was estimated using only data below 120 K and above 260 K, considering a combination of polynomial and linear functions. Thus, the dashed line in the *Cp* vs. *T* curve of Figure 5.15 (left) represents an estimation of the normal heat capacity using the high and low temperature data. Subtracting the lattice heat capacity from the experimental curve yields the excess heat capacity $\Delta C_p$ associated with the spin transition (Figure 5.15). Integrating the excess heat capacity with respect to *T* yielded the enthalpy variation, $\Delta H$, associated with the

spin transition (5.66 KJ/mol). On the other hand, $\Delta S$ can be obtained from integrating $\Delta Cp$ with respect to $lnT$ which yields 30.5 J/molK. These values are reasonable for a gradual SCO at high temperatures.[17–19]

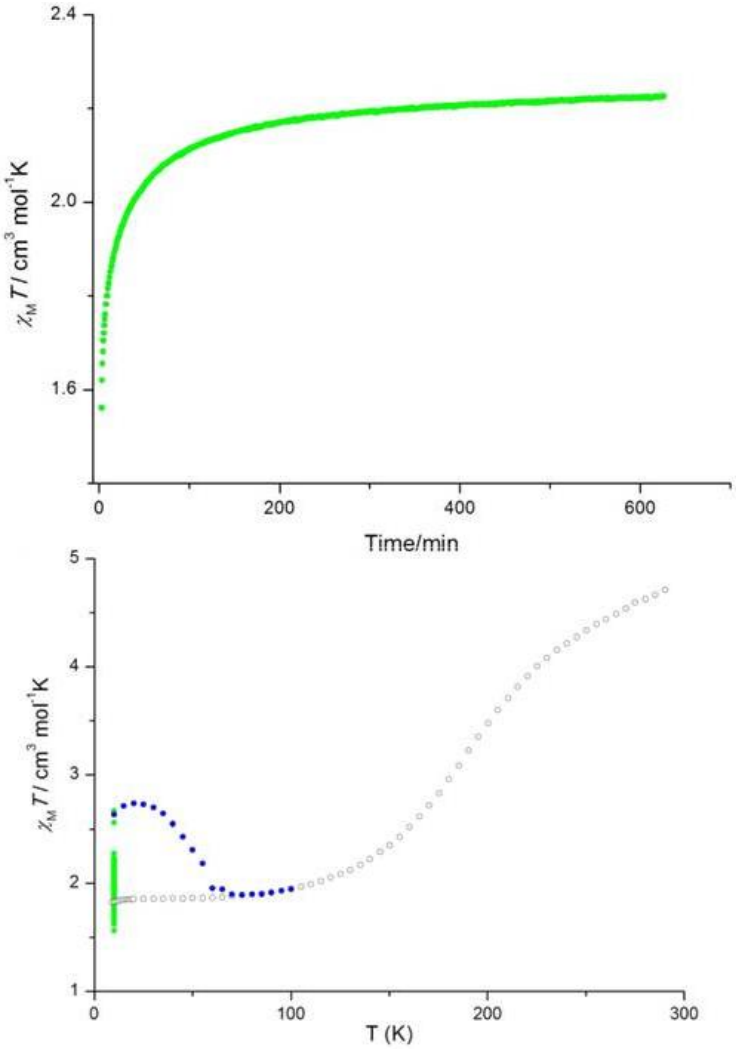


**Figure 5.16**: LIESST effect experiment of **11**. Top) time dependence of photo-induced $\chi_m T$ value under irradiation of green light. Bottom) $\chi_m T$ vs. $T$ plot of the experiment. Open gray circles represent the data upon cooling from room temperature. Green and blue circles represent the measurements through irradiation and thermal dependence after switching off the light, respectively.

## 5.8 LIESST Effect in $Cr(C_2O_4)_3 \subset [Fe_2(H_2L6)_3](BF_4)\cdot 1.4CH_3OH\cdot 6H_2O$ (11)

LIESST effect experiments were carried out on a 0.95 mg thin sample of compound **11** to investigate the posibility to trap the HS state of the Fe(II) centers at low temperatures. The sample was cooled to 10 K, and then it was irradiated with green light using a Xe

lamp and filters (500-650 nm) for 600 min. The $\chi_m T$ value increases through irradiation and reaches a saturated photo-induced value of 2.22 $cm^3mol^{-1}K$ (Figure 5.16). This increase corresponds to near 25 % of photo-induced conversion from [LS-LS] to [HS-LS] states, taking into account the ZFS splitting at this low temperature for the Cr(III) ion.

After switching off the light, the thermal relaxation of the meta-stable state was studied. The $\chi_m T$ value increases gradually upon heating, reaching a maximum value of 2.74 $cm^3mol^{-1}K$ at 20 K as a result of the magnetic anisotropy of the HS centers. Above 20 K, the $\chi_m T$ value starts to decrease due to the thermal relaxation of the excited-state centers, which is complete at 70 K. The behavior above this temperature reproduces that before irradiation. The $T_{LIESST}$ value estimated from the maximum of the derivative $d\chi_m T/dT$ of the thermal relaxation data is 55 K.

We discussed in chapter 3 the empirical formula ($T_{LIESST} = T_0 + 0.3T_{1/2}$)[19] which can be applied to Fe(II) iron complexes. Applying this formula on the compound **11** that exhibit LIESST effect gives $T_0$ values of 127 K. This value agrees with the data from the literature that shown that the three bidentate ligands show values around the straight line of $T_0$ value equal to 120 K.[28]

## 5.9 Dynamic (ac) Magnetic Properties of $Cr(C_2O_4)_3 \subset [Fe_2(H_2L6)_3](BF_4)\cdot 1.4CH_3OH\cdot 6H_2O$ (11)

The fact that the $Cr^{3+}$ ion is in an octahedral environment, well isolated in the cavity of the host and that its exhibits weak positive magnetic anisotropy associated with large transverse anisotropy suggests the possibility of slow magnetic relaxation effects characteristic of SIM. Therefore, dynamic (*ac*) magnetic susceptibility studies were performed on a polycrystalline sample of **11** at low temperatures.

At zero static magnetic field, no frequency dependence was observed up to 1000 Hz for $\chi_M'$ and $\chi_M''$ (in-phase and out-of-phase *ac* magnetic susceptibility component, respectively). This could be due to dominance of fast zero-field quantum tunneling of the magnetization through a potential thermal relaxation barrier.[20] Although the quantum tunneling of magnetization and direct relaxation processes are forbidden between Kramer's conjugates, non-perfect cancelation can be turned on as a result of dipolar or hyperfine interactions.[20,21] The application of a dc magnetic field can reduce

the quantum tunneling efficiency by removing the degeneracy of the levels of opposite directions of magnetic moment.[22]

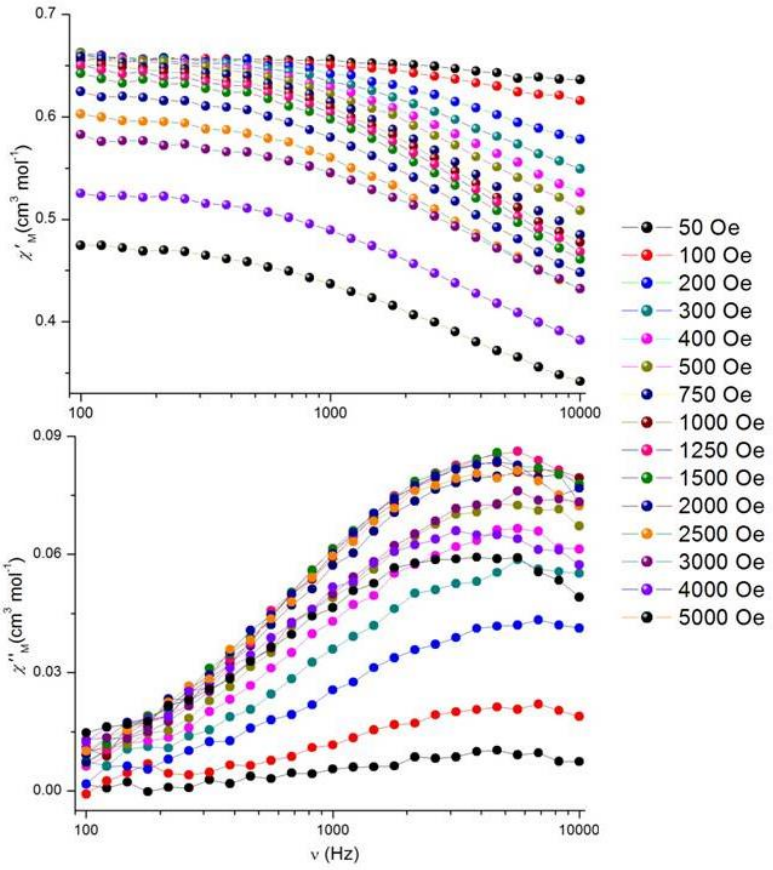


**Figure 5.17**: In-phase $\chi_M'$ (top) and out-of-phase $\chi_M''$ (bottom) components of the *ac* magnetic susceptibility collected for **11** under different static dc field at 2 K. Solid lines are guides for the eye.

For **11**, applying a static dc field as low as 200 Oe gives rise to maxima in the $\chi_M''$ susceptibility *vs.* Frequency plots at 2 K (Figure 5.17) accompanied by a decrease in the in-phase part of the susceptibility $\chi_M'$ at higher frequency. Applying a stronger external *dc* filed shifts the maxima to lower frequencies. However, in the range 750-2000 Oe no significant shift was observed. The characteristic pattern of both $\chi_M'$ and $\chi_M''$ indicates the slow relaxation of the magnetization typically seen in SMM species. The $\chi_M''$ *vs.* frequency data was fitted to the Cole-Cole function for the imaginary susceptibility (Cole-Cole model[23]) to determine the dc field dependence of the magnetic relaxation time $\tau$ (Figure 5.19). $\tau$ increases with increasing the *dc* magnetic field from 50-2000 Oe and then suddenly decreases. This decrease is followed by another increase of the relaxation time. Increasing the field split the degeneracy of the ground states and thus

reduces the degree of mixing and the quantum tunneling relaxation process. This induces the slow relaxation of the magnetization as the reversal of the direction of the magnetic moment need to take place through the thermal activation barrier. Another parameter that we can look at it in the Cole-Cole model is the $\beta$ parameter which indicates the distribution of the relaxation times where the value 1 indicates a single relaxation process. The values were in the range 0.748-0.759 and indicate the presence of reasonable distribution of relaxation times likely arising from inhomogeneities in the sample.

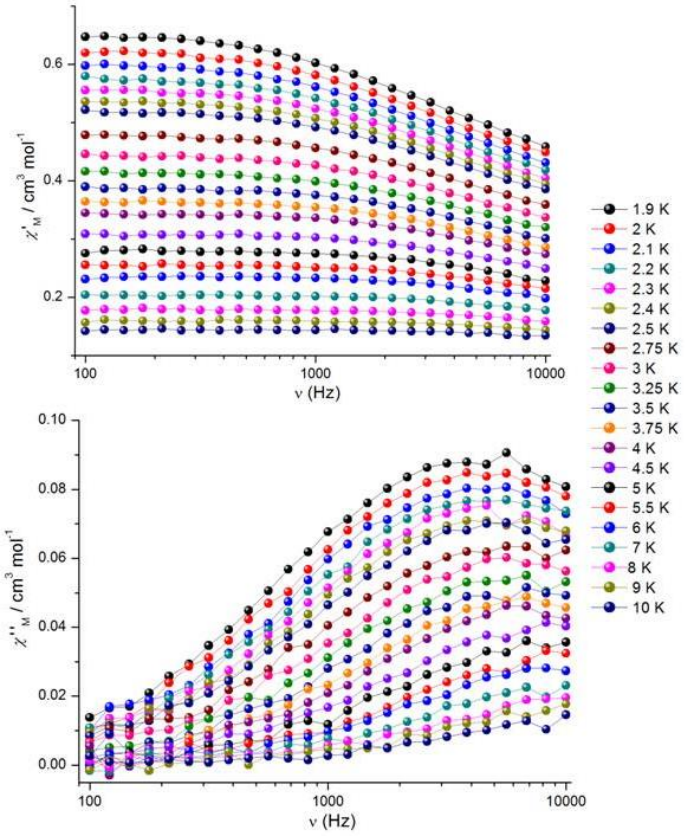


**Figure 5.18**: In-phase $\chi_M'$ (top) and out-of-phase $\chi_M''$ (bottom) components of the *ac* magnetic susceptibility as a function of the frequency collected for **11** under different temperatures (under *dc* magnetic field of 1000 Oe). Solid lines are guides for the eye

As there is no clear maximum in the field dependence of $\tau$, the frequency dependences of $\chi_M'$ and $\chi_M''$ were measured under a constant dc field of 1000 Oe over the temperature range 1.9-10 K (Figure 5.18). Clear maxima start to appear in the out-of-phase component of the magnetic susceptibility below 6 K, which shifting to lower frequencies with lowering the temperature. The deduced relaxation time from the Cole-Cole model[23] for the imaginary susceptibility $\chi_M''$ were used to construct the Arrhenius

plot $ln\tau$ *vs.* $T^{-1}$ (Figure 5.20). This plot exhibits a clear deviation from linearity. In the case of linear dependent of the relaxation time on the temperature the relaxation would follow the thermally activated mechanism (Orbach relaxation process). Arrhenius law would be valid [$\tau = \tau_0 e^{(U/k_BT)}$] and the slope would correspond to the effective spin reversal barrier *U* while the y-intercept is the attempt relaxation time $\tau_0$. For **11**, fitting the high temperature data over 6 K where it shows a fair linearity, yielded *U* = 13.38 $cm^{-1}$ and $\tau_0 = 4.18\times10^{-6}$ s (*R*=0.9999). Since a positive *D* value was observed form the *dc* magnetic study with high in-plane anisotropy (*E*/*D* = 0.556), the slow relaxation will be as a result of easy plane and the energy barrier will arise from the *E* parameter with a maximum value of $U = |E|(S^2 - 1/4)$, which equals 0.692 $cm^{-1}$. The energy barrier value deduced from the linear fitting of high temperatures is significantly higher than the expected one. This indicates that the Orbach process is not the dominant relaxation process even at high temperatures. Moreover, the curvature of the Arrhenius plot indicates the involving of different relaxation processes. This could include the Raman and direct temperature dependent processes in addition to the quantum tunneling mechanism[24,25] (temperature independent) as seen in equation 1.

$$\tau^{-1} = \tau_0{}^{-1} e^{(-U/k_BT)} + CT^m + AT^n + \Gamma_{QTM} \qquad 1$$

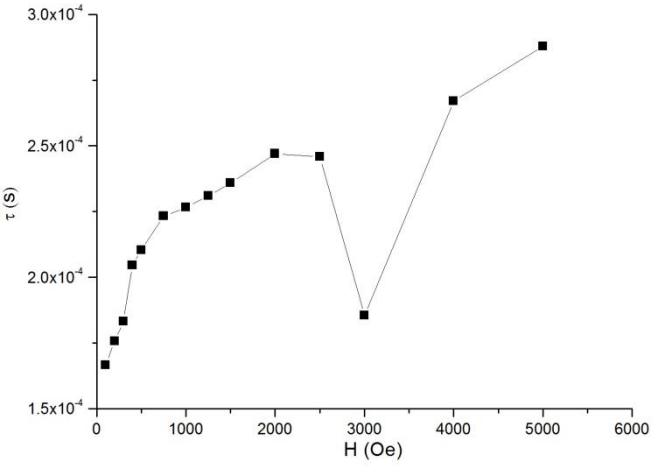


**Figure 5.19**: Field dependence of the magnetic relaxation time, $\tau$, at 2 K for **11**. Solid lines are guides for the eye.

A reasonable simulation can be obtained only involving the first two terms. The best fit yields *C* = 289.10 $s\text{-}1K^{-2}$, $\tau_0 = 2.67\times10^{-4}$ s, *U* = 0.36 $cm^{-1}$ with *m* = 2. The *m* value could deviate from the expected one of Kramer ion (*m* = 9) depending on the system

and have a value between 1 and 9.[26–30] The high $\tau_0$ value compared to the one seen in SIM systems[31] could indicate that quantum tunneling is active even at higher temperatures or that the relaxation process does not involve any thermal Orbach mechanism. However, the experimental data could be fitted also without including the Orbach thermal process and involving only a Raman process in addition to consider a temperature independent relaxation mechanism[32,33] (*i.e* the second and the forth terms in equation 1). The best fit then gives $C$ = 297.58 $s^{-1}$, $\Gamma_{QTM}$ = 3025.50 $s^{-1}$ with $m$ = 2. This agrees with what was shown by Gomez-Coca et. al.[21] for Kramer's ions with non-uniaxial anisotropy where the relaxation is dominant by Raman mechanism but with the presence of direct processes at low temperatures due to the presence of hyperfine interactions that yield a non-perfect cancelation of the latter processes. In the case of **11**, the relative low D value and the probable intermolecular interactions of the ion centers could allow such quantum tunneling processes at low temperatures.

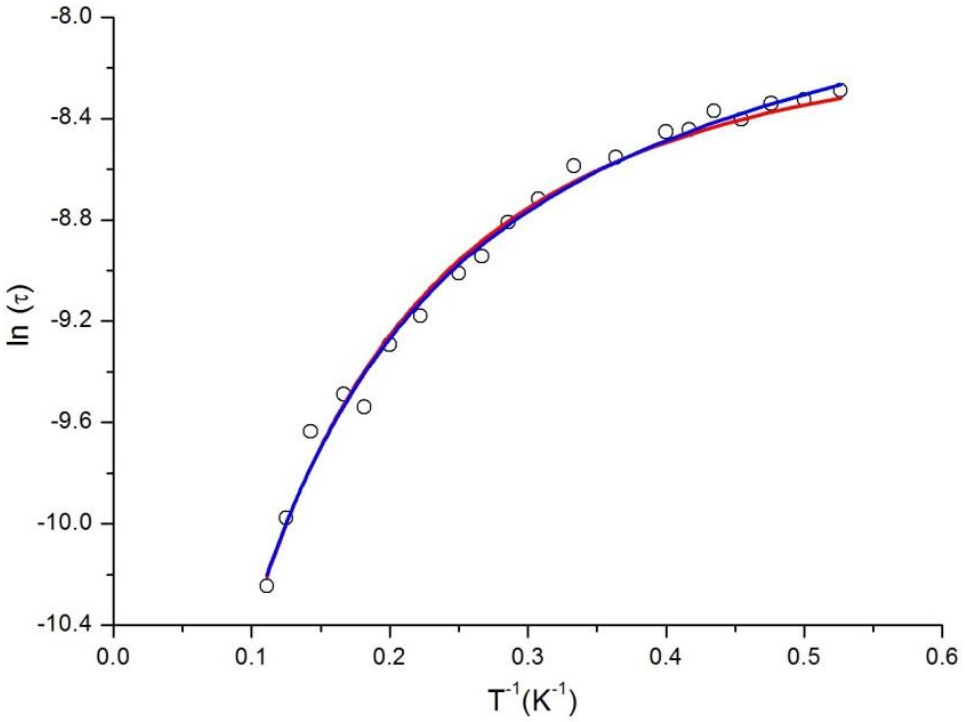


**Figure 5.20**: Arrhenius plot of the temperature dependence of $\tau$ (open circles) with the best fit obtained using neither the expression $\tau^{-1} = {\tau_0}^{-1} e^{(-U/k_B T)} + CT^m$ (blue) or $\tau^{-1} = CT^m + \Gamma_{QTM}$ (red), see text for details.

## 5.10 Mass Spectrometry of $Cr(C_2O_4)_3\subset[Fe_2(H_2L6)_3](BF_4)\cdot 1.4CH_3OH\cdot 6H_2O$ (11)

The mass spectrum of **11** was conducted in DMF-$CH_3CN$ solution using the positive ion electrospray ($ESI^+$) technique (Figure 5.21). The peak correspond to the cationic encapsulated helicate $\{Cr(C_2O_4)_3\subset[Fe_2(H_2L6)_3]\}^+$ was observed at m/z = 1749.27. Another peak with 2+ charge was detected at m/z = 875.14 where the helicate is protonated with one proton to give $\{Cr(C_2O_4)_3\subset[Fe_2(H_2L6)_3] + H\}^{2+}$. Figure 5.22 illustrate the match of the theoretical and the experimental isotropic distributions of the latter peak. This indicates that the host-guest system with encapsulated $Cr(C_2O_4)_3^{3-}$ is stable in solution even though in high polar solvent like DMF.

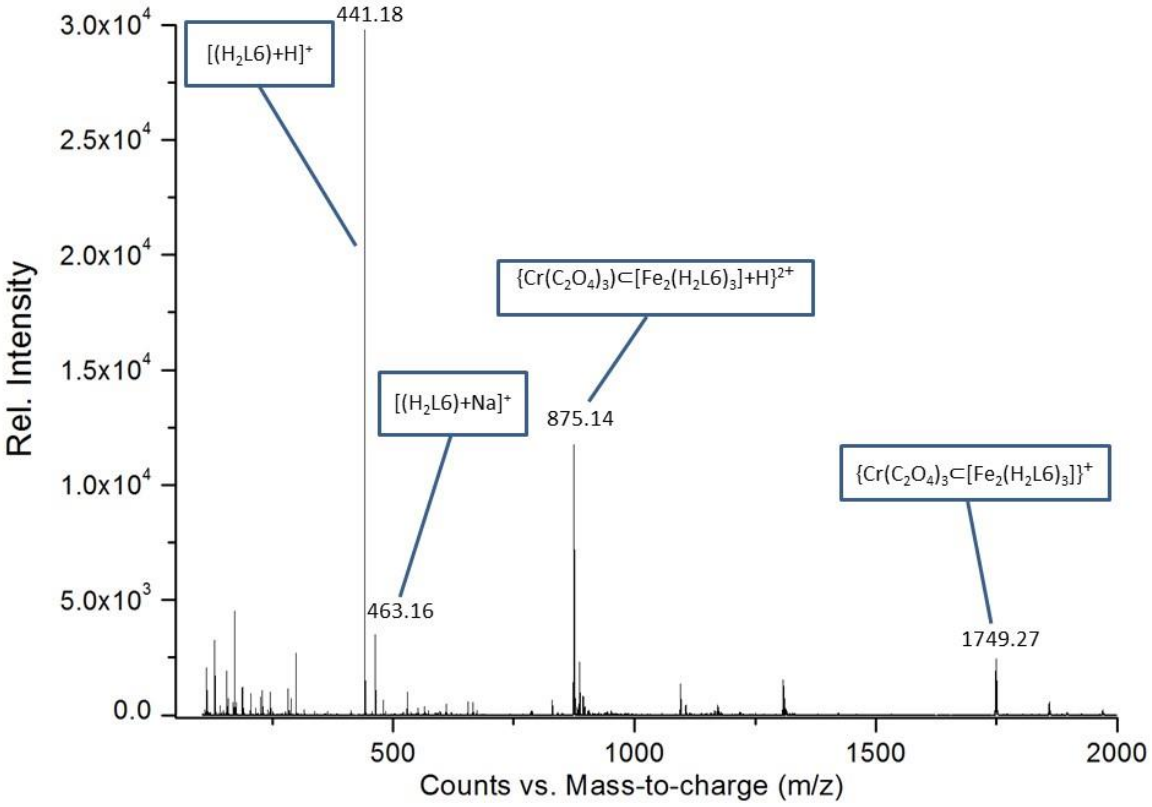


Figure 5.21: Mass spectrum of **11** in DMF-$CH_3CN$ mixture with identification of the important peaks.

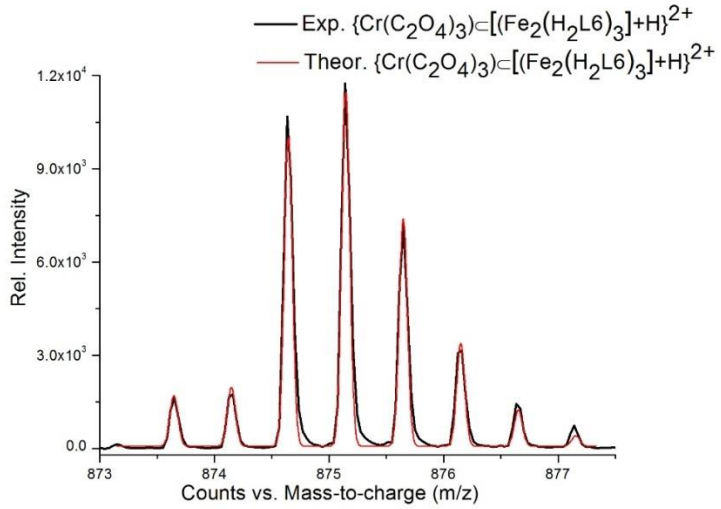


Figure 5.22: The match of theoretical and experimental isotopic distribution of the encapsulated helicate peaks$\{Cr(C_2O_4)_3\subset[Fe_2(H_2L6)_3] + H\}^{2+}$.in **11**.

## 5.11 Conclusion

Ligands $H_2L6$ was used to self-assembly of dinuclear triple stranded helicates with encapsulate metal oxalate inside its cavity $[M(C_2O_4)_3\subset Fe_2(H_2L6)_3]^+$ where M = Fe(III) or Cr(III) ions. This considered as novel example of encapsulation of metal complex inside small cage like triple stranded helicate. In the case of encapsulated chromium oxalate $[Cr(C_2O_4)_3]^{3-}$, the Fe(II) centers exhibit SCO and LIESST effect from [LS-LS] to [HS-LS] states. On the other hand, the encapsulated Cr(III) ion exhibits SIM-like behavior. This make the complex as unique example of host-guest system where both LIESST and SIM behavior are coexist. This opens the door to the possibility of manipulating the SIM properties of the Cr(III) center via the LIESST effect on the host component of the molecular assembly, since both effects may be implemented at the same temperature range.

## 5.12 Experimental

**$Fe(C_2O_4)_3\subset[Fe_2(H_2L6)_3](BF_4)\cdot 4CH_3OH\cdot 3.7H_2O$ (10).** A suspension of $H_2L6$ (25 mg, 0.057 mmol) in methanol (10 mL) was added dropwise to 10 ml methanolic solution of $Fe(BF_4)_2.6H_2O$ (38.5 mg, 0.114mmol) and 15 mg of ascorbic acid. A red solution formed which was stirred for 1 hour and then filtered off. The resulted solution was combined with 15 ml acetonitrile and then left for slow evaporation which yieldedred crystals after two week. The yield was 6.1 mg (14.2 %). *Anal. Calc.* (Found) for **10 (-**

**$3CH_3OH$, $+H_2O$)**: C, 54.03 (54.28); H, 3.30 (3.67); N, 12.33 (12.52).ESI-MS: m/z 1753.28 $\{Fe(C_2O_4)_3\subset[Fe_2(H_2L6)_3]\}^+$, m/z 876.64 $\{Fe(C_2O_4)_3\subset[Fe_2(H_2L6)_3)] + H\}^{2+}$.

**$Cr(C_2O_4)_3\subset[Fe_2(H_2L6)_3](BF_4)\cdot 1.4CH_3OH\cdot 6H_2O$ (11).** Under inert conditions, a suspension of $H_2L6$ (25 mg, 0.057 mmol) in methanol (10 mL) was added dropwise to 5 ml methanolic solution of $Fe(BF_4)_2.6H_2O$ (12.83 mg, 0.038 mmol). A red solution formed which was stirred for 1 hour and then filtered off. The resulted solution was layered with aqueous solution (10 ml) of $K_3Cr(C_2O_4)_3.3H_2O$ (9.3 mg, 0.019 mmole) which yielded orange-red crystals after two week. The yield was 10.5 mg ( %). *Anal. Calc.* (Found) for **11 (-1.4 $CH_3OH$)**: C, 55.66 (55.60); H, 3.68 (3.73); N, 13.11 (12.97).ESI-MS: m/z1749.27 $[Cr(C_2O_4)_3\subset Fe_2(H_2L6)_3]^+$, m/z 875.14 $[(Cr(C_2O_4)_3\subset Fe_2(H_2L6)_3) + H]^{2+}$.

## 5.13 References


1 M. Yoshizawa, K. Ono, K. Kumazawa, T. Kato and M. Fujita, *J. Am. Chem. Soc.*, 2005, **127**, 10800–10801.

2 K. Ono, M. Yoshizawa, T. Kato and M. Fujita, *Chem. Commun. (Camb).*, 2008, **1**, 2328–2330.

3 K. Ono, M. Yoshizawa, M. Akita, T. T. Kato, Y. Tsunobuchi, S. I. Ohkoshi, M. Fujita, M. Yoshlzawa, M. Aklta, T. T. Kato, Y. Tsunobuchl, S. I. Ohkoshi and M. Fujita, *J. Am. Chem. Soc.*, 2009, **131**, 2782–2783.

4 C. Y. Su, Y. P. Cai, C. L. Chen, F. Lissner, B. S. Kang and W. Kaim, *Angew. Chemie - Int. Ed.*, 2002, **41**, 3371–3375.

5 B. Therrien, *Chem. - A Eur. J.*, 2013, **19**, 8378–8386.

6 B. Therrien, G. Süss-Fink, P. Govindaswamy, A. K. Renfrew and P. J. Dyson, *Angew. Chemie*, 2008, **120**, 3833–3836.

7 J. E. M. Lewis, E. L. Gavey, S. a. Cameron and J. D. Crowley, *Chem. Sci.*, 2012, **3**, 778.

8 G. H. Clever, W. Kawamura, S. Tashiro, M. Shiro and M. Shionoya, *Angew. Chemie - Int. Ed.*, 2012, **51**, 2606–2609.

9 C. Desmarets, G. Gontard, A. L. Cooksy, M. N. Rager and H. Amouri, *Inorg. Chem.*, 2014, **53**, 4287–94.

10 X. Feng, C. Mathonière, I.-R. Jeon, M. Rouzières, A. Ozarowski, M. L. Aubrey, M. I. Gonzalez, R. Clérac and J. R. Long, *J. Am. Chem. Soc.*, 2013, **135**, 15880–15884.

11 C. Mathonière, H. J. Lin, D. Siretanu, R. Clérac and J. M. Smith, *J. Am. Chem. Soc.*, 2013, **135**, 19083–19086.

12 A. L. Spek, *Acta Crystallogr. Sect. C, Struct. Chem.*, 2015, **71**, 9–18.

13 U. Hannover, A. Chemie and D.- Hannover, *Zeitschrift für Krist. - New Cryst. Struct.*, 1997, **0010**, 83–84.

14 D. Taylor, *Aust. J. Chem.*, 1978, **31**, 1455 – 1462.

15 R. L. Carlin, *Magnetochemistry*, Springer-Verlag Berlin Heidelberg, 1st edn., 1986.

16 R. Boca, *Coord. Chem. Rev.*, 2004, **248**, 757–815.

17 M. Sorai, M. Nakano and Y. Miyazaki, *Chem. Rev.*, 2006, **106**, 976–1031.

18 Z. Arcis-Castíllo, S. Zheng, M. a. Siegler, O. Roubeau, S. Bedoui and S. Bonnet, *Chem. - A Eur. J.*, 2011, **17**, 14826–14836.

19 O. Roubeau, M. Castro, R. Burriel, J. G. Haasnoot and J. Reedijk, *J. Phys. Chem. B*, 2011, **115**, 3003–3012.

20 D. Gatteschi and R. Sessoli, *Angew. Chemie-International Ed.*, 2003, **42**, 268–297.

21 S. Gómez-Coca, A. Urtizberea, E. Cremades, P. J. Alonso, A. Camón, E. Ruiz and F. Luis, *Nat. Commun.*, 2014, **5**, 4300.

22 D. Gatteschi, R. Sessoli and J. Villain, *Molecular Nanomagnets*, Oxford University Press, 2006.

23 R. H. Cole, K. S. and Cole, *J. Chem. Phys.*, 1941, **9**, 341–351.

24 J. M. Zadrozny, M. Atanasov, A. M. Bryan, C.-Y. Lin, B. D. Rekken, P. P. Power, F. Neese and J. R. Long, *Chem. Sci.*, 2013, **4**, 125–138.

25 K. R. Meihaus, S. G. Minasian, W. W. Lukens, S. A. Kozimor, D. K. Shuh, T. Tyliszczak and J. R. Long, *J. Am. Chem. Soc.*, 2014, **136**, 6056–6058.

26 A. Singh and K. N. Shrivastava, *Phys. Status Solidi*, 1979, **95**, 273–277.

27 K. N. Shrivastava, *Phys. Status Solidi*, 1983, **117**, 437–458.

28 R. Herchel, L. Váhovská, I. Potocnak and Z. Trávnícek, *Inorg. Chem.*, 2014, **53**, 5896–5898.

29 E. Colacio, J. Ruiz, E. Ruiz, E. Cremades, J. Krzystek, S. Carretta, J. Cano, T. Guidi, W. Wernsdorfer and E. K. Brechin, *Angew. Chemie Int. Ed.*, 2013, **52**, 9130–9134.

30 V. V. Novikov, A. a. Pavlov, Y. V. Nelyubina, M.-E. Boulon, O. a. Varzatskii, Y. Z. Voloshin and R. E. P. Winpenny, *J. Am. Chem. Soc.*, 2015, **137**, 9792–9795.

31 G. A. Craig and M. Murrie, *Chem. Soc. Rev.*, 2015, **44**, 2135–2147.

32 K. S. Pedersen, L. Ungur, M. Sigrist, A. Sundt, M. Schau-Magnussen, V. Vieru, H. Mutka, S. Rols, H. Weihe, O. Waldmann, L. F. Chibotaru, J. Bendix and J. Dreiser, *Chem. Sci.*, 2014, **5**, 1650.

33 P.-E. Car, A. Favre, A. Caneschi and R. Sessoli, *Dalt. Trans.*, 2015, **44**, 15769–15773.